

Diagnostics of the Coronal Hole and the adjacent Quiet Sun by *The Hinode/EUV Imaging Spectrometer* (EIS)

P. Kayshap¹ · D. Banerjee^{2,3} · A. K. Srivastava⁴

© Springer ●●●

Abstract A comparison between a Coronal Hole (CH) and the adjacent Quiet-Sun (QS) has been performed using the spectroscopic diagnostics of *Hinode/ the EUV Imaging Spectrometer* (EIS). Coronal funnels play an important role in the formation and propagation of the nascent fast solar wind. Applying Gaussian fitting procedures to the observed line profiles, Doppler velocity, intensity, line width (FWHM) and electron density have been estimated over CH and adjacent QS region of a North Polar Coronal Hole (NPCH). The aim of this study is to identify the coronal funnels based on spectral signatures. Excess width regions (excess FWHM above a threshold level) have been identified in QS and CH. The plasma flow inversion (average red-shifts changing to blue-shifts at a specific height) in CH and excess width regions of QS take place at $\sim 5.01 \times 10^5$ K. Furthermore, high density concentration in excess width regions of QS provides an indication that these regions are the footprints of coronal funnels. We have also found that non-thermal velocities of CH are higher in comparison to QS confirming that the CHs are the source regions of the fast solar wind. Doppler and non-thermal velocities as recorded by different temperature lines have been also compared with previously published results. As we go from lower to upper solar atmosphere, down-flows are dominated in lower atmosphere while coronal lines are dominated by up-flows with a maximum value of $\sim 10\text{--}12$ km s⁻¹ in QS. Non-thermal velocity increases first but after $\text{Log } T_e = 5.47$ it decreases further in QS. This trend can be interpreted as a signature of the dissipation of Alfvén waves, while increasing trend as reported earlier may attribute to

¹ Aryabhata Research Institute of Observational Sciences (ARIES), Manora Peak, Nainital-263002, India
email: pradeep.kashyap@aries.res.in

² Indian Institute of Astrophysics (IIA), Bangalore-560034, India
email: dipu@iiap.res.in

³ CESSI, Indian Institute of Science Education and Research, Kolkata, Mohanpur - 741252, India
email: dipu@iiap.res.in

⁴ Department of Physics, Indian Institute of Technology (Banaras Hindu University), Varanasi-221005
email: asrivastava.aap@iitbhu.ac.in

the signature of the growth of Alfvén waves at lower heights. Predominance of occurrence of nano-flares around O VI formation temperature could also explain the non-thermal velocity trend.

Keywords: Coronal Holes; Alfvén waves; Spectral Line, Diagnostics

1. Introduction

Coronal Holes (CHs; Waldmeier 1975) are the regions on the Sun, which appear dark in comparison to the quiet-Sun (QS) because they emit less in UV & X-rays and maintained at a lower temperature than the surroundings. The different magnetic structures of QS and CH are responsible for their different appearance in coronal lines (Wiegmann and Solanki, 2004). CHs are dominated by coronal funnels, which originate from the adjoining locations of super-granule boundaries at the photosphere and expand abruptly towards higher atmosphere (Gabriel, 1976; Axford and McKenzie, 1997; Marsch and Tu, 1997; Hackenberg, Mann, and Marsch, 1999). QS regions are dominated by closed magnetic field lines. Although, QS has also the coronal funnels with less expansion. The filling factors of these coronal funnels are less in QS compared to CHs. Coronal funnels play an important role in the formation as well as propagation of nascent fast solar wind in the CHs (Tu *et al.*, 2005; He, Tu, and Marsch, 2008; Tian *et al.*, 2010). Spectroscopic analysis is important to understand the dynamics of the QS as well as CH. The Doppler velocity, which provides important information to any model of solar coronal heating, has a tendency to invert from pre-dominant red-shifts (*i.e.*, downflows) to blue-shifts (*i.e.*, upflows) as we go higher from chromosphere to corona in CHs (Warren, Mariska, and Wilhelm, 1997; Hassler *et al.*, 1999; Peter and Judge, 1999; Peter, 1999; Xia, Marsch, and Curdt, 2003) as well as in QS (Chae, Yun, and Poland, 1998; Peter and Judge, 1999; Teriaca, Banerjee, and Doyle, 1999a; Dadashi, Teriaca, and Solanki, 2011). Several possible mechanisms have been proposed to explain the observed red-shifts of the solar transition region (TR) and coronal lines, *e.g.*, return of spicular material (Pneuman and Kopp, 1978; Athay, 1984), downward propagating acoustic waves (Hansteen, 1993; Hansteen, Maltby, and Malagoli, 1997; Teriaca, Banerjee, and Doyle, 1999a). The turnover temperature from red-shift to blue-shift is a crucial observational parameter for future modelling.

Full-width-at-half-maximum (FWHM) is also an important parameter to understand the dynamics of QS and CH. Some observed solar Extreme-ultraviolet (EUV) and Far-ultraviolet (FUV) spectral line profiles are found to be broader than those expected from thermal broadening (Boland *et al.*, 1975; Doschek *et al.*, 1976; Mariska, Feldman, and Doschek, 1978; Banerjee *et al.*, 1998). These excess widths, after subtracting thermal and instrumental widths from the observed widths, are called as non-thermal widths. Non-thermal velocities as derived from these widths reveal the presence of non-thermal motions/unresolved flows or the presence of waves in the solar atmosphere. Early studies show that the non-thermal velocities increase within a narrow range of temperature (from chromosphere up to TR temperatures) in the QS near disk centre (Doschek *et*

al., 1976; Mariska, Feldman, and Doschek, 1978; Dere and Mason, 1993)). After the launch of Solar Ultraviolet Measurements of Emitted Radiation (SUMER) on board SoHO, the non-thermal velocity has been investigated for a quite large range of solar atmosphere (*i.e.*, 10^4 K to 2×10^6 K). It is found that initially non-thermal velocity increases but after a certain temperature decreases corresponding to coronal heights in QS as well as active regions (Chae, Schühle, and Lemaire, 1998; Teriaca, Banerjee, and Doyle, 1999a; Doschek and Feldman, 2000; Peter, 2001; Patsourakos and Klimchuk, 2006; Doschek *et al.*, 2007)). Several mechanisms have been proposed to interpret the pattern of non-thermal velocity through the solar atmosphere, *e.g.*, MHD wave models or magnetic reconnection generated turbulence (Doschek *et al.*, 1976; Mariska, Feldman, and Doschek, 1978), unresolved laminar flows, waves and turbulent flows (Chae, Yun, and Poland, 1998), Alfvén waves (Peter, 2001), *etc.* Recently, Coyner and Davila (2011) have shown that the non-thermal velocities represent strong distribution from 19 km s^{-1} to 22 km s^{-1} in the various parts of the solar atmosphere.

In the present study, we have performed a comparison between QS and CHs on the basis of various spectral parameters (*e.g.*, Doppler velocity, non-thermal width, *etc.*). On the basis of the variations of these parameters and density contrast, we have located the most probable regions of coronal funnels in QS. Variation of the non-thermal velocity and average Doppler velocity with temperature have also been investigated in QS by including some previous relevant results with our estimated values. The present work is organized as follows. In Section 2, we describe the details about the observation and data reduction. Results related to the comparison between QS and CH as well as identification of the coronal funnels are presented in Section 3. Section 4 outlines the temperature dependent behaviour of non-thermal velocity in QS and CH. Discussion and Conclusions are presented in the last section.

2. Observations and Data Reduction

Extreme Ultraviolet Imaging Spectrometer (EIS) on board *Hinode* spacecraft is a normal-incidence EUV spectrometer. EIS has spatial resolution of ~ 2 -arcsecond and high spectral resolution of 0.0223 \AA per pixel. EIS observes high resolution spectra in short wavelength band (*i.e.*, $170 - 211 \text{ \AA}$) and long wavelength band (*i.e.*, $246 - 292 \text{ \AA}$). Four types of slits/slots (*e.g.*, 1-, 2-, 40-, 256-arcsecond) are available in the EIS observations (Culhane *et al.*, 2007). A North Polar Coronal Hole (NPCH) observation captured on 10 October 2007 by *Hinode*/EIS, has been used in the present work. The observed region (FOV) is marked as a white rectangular box on the SoHO/EIT 195 \AA image (*cf.*, Figure 1). NPCH was observed using the 2-arcsecond slit in the raster mode for more than four hours (*i.e.*, from 14:03 UT to 18:17 UT) by capturing 101 exposures with 155 s exposure time on each scanning step. This very long exposure (*i.e.*, 155 second) enhances the count statistics, therefore, this data set is reliable for deriving various line parameters (*e.g.*, Doppler velocity, FWHM, *etc.*) from the line profiles and also ideal for density diagnostics. Standard *Hinode*/EIS routine `eis_prep.pro`, which is available in SolarSoft (SSW) package, has been used for the calibration of raw

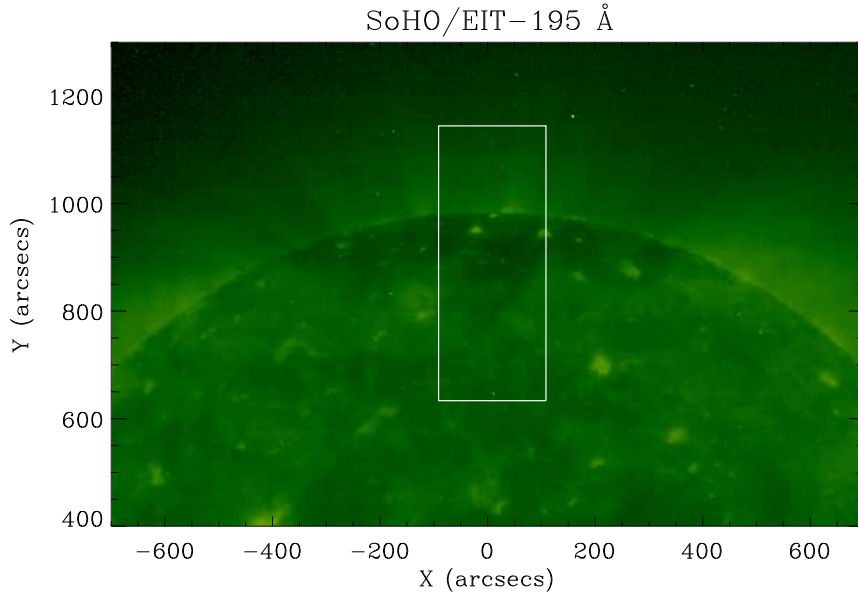


Figure 1. White rectangular box marks the FOV of the observed region of *Hinode*/EIS, over-plotted on the SoHO/EIT 195 Å image. This North Polar Coronal Hole (NPCH) was observed by *Hinode*/EIS from 14:13 UT to 18:17 UT on 10 October 2007.

Table 1. This table shows all the four lines, which are used in the present analysis. Formation temperatures as well as the standard wavelengths are also listed.

Sr. No.	Ion	Wavelength (Å)	Log T (K)
1	Si VII	275.35	5.8
2	Fe X	184.54	6.0
3	Fe XII	195.12	6.1
4	Fe XIII	202.04	6.2

data. This routine converts original raw data into physical data after processing various necessary steps, *e.g.*, subtraction of the dark current, removal of cosmic rays and hot pixels and radiometric calibration, *etc.* Four spectral lines have been used in the present analysis as listed in Table 1. Si VII 275.35 Å, Fe X 184.54 Å and Fe XIII 202.04 Å lines are comparatively clean lines and are not affected by blending issues (Young *et al.*, 2007), while Fe XII 195.120 Å is blended with Fe XII 195.180 Å (Young *et al.*, 2009). Although, Young *et al.* (2009) have shown that Fe XII 195.120 Å is not affected appreciably by Fe XII 195.180 Å line in the coronal holes, however, we have considered this blending and removed it in the present analysis. Various instrumental effects related to the *Hinode*/EIS observations (*e.g.*, slit tilt, thermal variation, EIS CCD offset) must be addressed before the Gaussian fitting to derive the basis parameters from the observed line profiles. *Hinode*/EIS has single grating that disperse the light onto two CCDs

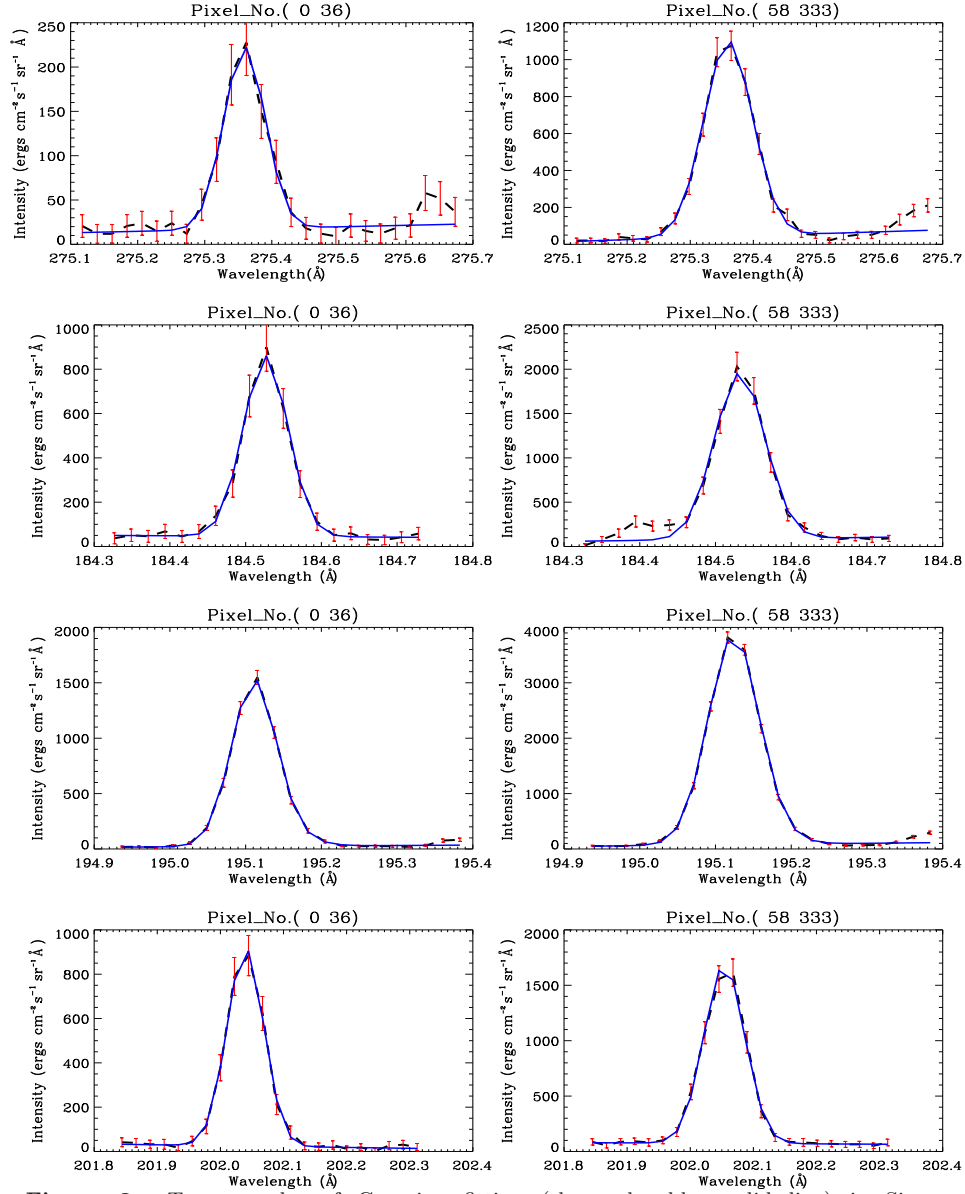


Figure 2. Two samples of Gaussian fitting (shown by blue solid line) in Si VII 275.35 \AA (top-row), Fe X 184.54 \AA (second-row), Fe XII 195.120 \AA (third-row) and Fe XIII 202.04 \AA (bottom-row) have been shown in this figure. The locations of these two displayed Gaussian fitting samples in each line profile correspond to the pixel (0,36) and pixel (58,333). The standard 1- σ error is also overplotted by red color in each sample fit.

and spatial offset is present between these two CCDs of the *Hinode*/EIS. We have used standard *Hinode*/EIS routine, `eis_ccd_offset.pro`, to find out the pixel offset and direction of the offset (*i.e.*, up or down) in all lines relative to the He II 256.32 Å. After finding the amount and direction of the shift, we have shifted the observed spectra by that many pixels in the corresponding direction in all the lines. After that, we have selected a common region in all four lines for further analysis. To measure the thermal drift, we have used the same technique as Tian *et al.* (2010) have used in his analysis. After calculating slit tilt by using `eis_slit_tilt.pro` standard *Hinode*/EIS routine, we have built a wavelength correction offset array (*i.e.*, for wavelength correction) for all four lines. These wavelength offset arrays have the combined effect of slit tilt as well as thermal drift of respective spectral line. We have fitted a single Gaussian function on the three line profiles (*i.e.*, Si VII, Fe X and Fe XIII). Double Gaussian has been fitted on the Fe XII line profile to separate the Fe XII 195.180 Å component from Fe XII 195.12 Å line profile. The combined effect of the slit tilt and orbital variation for any spectral line has been removed (wavelength vector corrected by applying wavelength correction offset array at each pixel of the observed region) before the Gaussian fitting in the chosen spectral line profile.

For the double Gaussian fitting (*i.e.*, in case of Fe XII 195.120 Å), we have used the procedure of Young *et al.* (2009). Figure 2 represents the two samples of Gaussian fit in each line profile at two different locations. From the Gaussian fitting, we have extracted the basic parameters (*i.e.*, intensity, Gaussian sigma, line centroid, etc.) at each location (pixels) of the commonly observed region. Rest wavelength measurement is difficult task as the absolute wavelength calibration is not available for *Hinode*/EIS. Unfortunately, any low temperature chromospheric line is not present in our wavelength window, therefore, in the present case we have used the Limb method (Peter and Judge, 1999) for measuring the rest wavelengths. After measuring the rest wavelengths in each line profile, we have estimated the Doppler velocity at each location of the observed region. Similarly, we have estimated the FWHM from Gaussian sigma (*i.e.*, $\text{FWHM}=2.3548\sigma$) over commonly observed region. The intensity, Doppler velocity and FWHM maps are shown in Figure 3 corresponding to all the four lines. Apart from the Doppler velocity, intensity and FWHM, electron density can also be estimated with the help of intensity ratio of two density sensitive lines and CHIANTI database (Dere *et al.*, 1997; Landi *et al.*, 2006). In the present analysis, we have used Fe XII 186.88 Å and Fe XII 195.120 Å for the density measurement, which represents the density at coronal heights. Young *et al.* (2009) have shown that both density sensitive Fe XII lines suffer from the blending problem (*i.e.*, Fe XII 186.88 Å with S XI 186.839 Å and Fe XII 195.120 Å with Fe XII 195.180 Å). The intensity contribution of S XI 186.839 Å in Fe XII 186.88 Å intensity can be assessed from the S XI 188.617 Å or S XI 191.266 Å. On the basis of active region datasets, Young *et al.* (2009) have shown that S XI 186.839 Å can contribute maximum 5% intensity in Fe XII in the regime of moderate densities while S XI 186.839 Å can contribute 2% intensity in Fe XII 186.88 Å in the regime of more higher densities. Unfortunately, any one transition out of these two S XI transitions is not present in the present data-set, therefore, we have assumed that S XI 186.839 Å contributes 5% in the

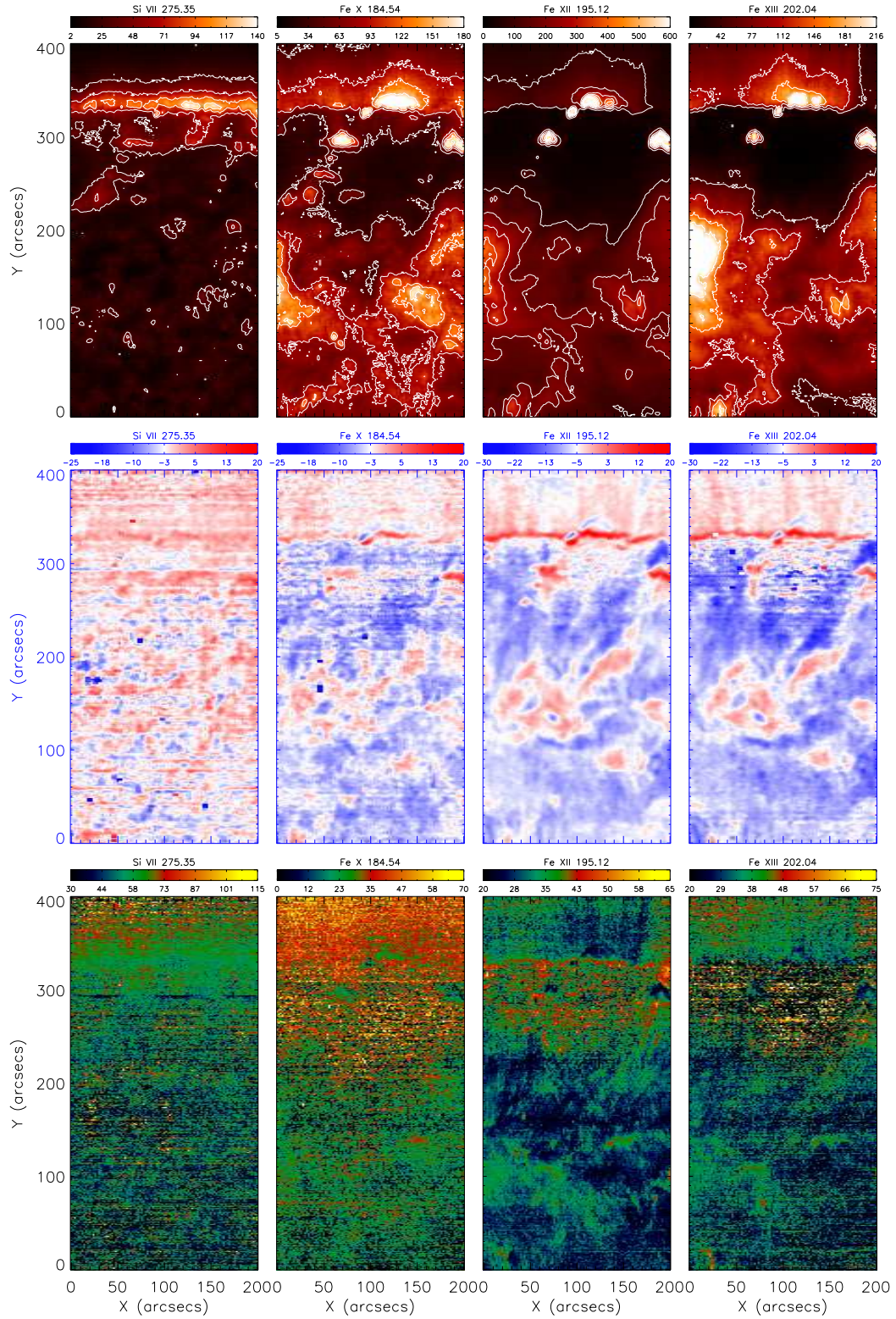


Figure 3. Intensity (top-row), Doppler velocity (middle-row) and FWHM (bottom-row) maps corresponding to the NPCH (as marked by a rectangular box in Figure 1) as observed by four lines, Si VII 275.5 Å, Fe X 184.54 Å, Fe XII 195.120 Å and Fe XIII 202.04 Å. Intensity contours are shown on the intensity maps.

Fe XII 186.88 Å intensity. Although, the assumption of the 5% contribution of S XI 186.839 Å in Fe XII 186.88 Å is based on the active region data-sets but we have used this value (i.e., 5% contribution) to remove the blending from Fe XII 186.88 Å in the present NPCH observation because the intensity contribution of S XI 186.839 Å is more effective towards the moderate densities in comparison to the very high densities (Young *et al.*, 2009). To remove the blending from Fe XII 195.120 Å line, we have followed the same approach as described by Young *et al.* (2009). After calculating the intensity ratio from these two density sensitive lines, we have derived the density over the observed common region (*cf.*, left panel of Figure 7). The density map (Figure 7) also represents the overplotted small boxes, which we have used for the present work and will be described in the upcoming section. We concentrated primarily on three regions in this work, which is shown by three dashed black boxes on the Doppler velocity map (Figure 4). These three regions represent quiet-Sun (QS; lower box), quiet-Sun with coronal hole boundary (QSCH; middle box) and coronal hole (CH; upper box) respectively. Measurement of the various plasma parameters have been evaluated for various localised regions that correspond to the three broadly classified physical regions as QS, QSCH and CH.

3. Comparison Between QS and CH Parameters

Ion temperature and unresolved non-thermal motions and/or presence of MHD waves are responsible for the spectral broadening of optically thin coronal emission lines in the solar atmosphere. Generally, it is assumed that ions and electrons are in the thermal equilibrium, although the temperature of the ions and electrons may be different from each other, particularly at extended part of the corona. But for the inner corona, we have assumed that ion temperature is identical to the electron temperature. FWHM can be expressed as follows,

$$FWHM = \left[W_{inst} + 4 \ln 2 \left(\frac{\lambda}{c} \right)^2 \left(\frac{2kT_i}{M_i} + \xi^2 \right) \right]^{1/2}, \quad (1)$$

where, T_i , M_i , ξ and W_{inst} are the ion-temperature, ion-mass, non-thermal velocity, and instrumental-width respectively. Instrumental, thermal and non-thermal widths are the three components of the observed FWHM. Instrumental as well as thermal (*i.e.*, at a particular ion formation temperature) width components are constant, therefore, the variations in the FWHM arise due to the variation in the non-thermal width. The non-thermal width provides signature of various unresolved small-scale dynamics in the solar atmosphere, which do not normally recorded by imaging instruments. Figure 4 shows the Doppler velocity map in Fe XII 195.120 Å line, which is overlaid with intensity contours. The disk part of the observed FOV is divided into three parts for further analysis, which is also marked on the Doppler velocity map and demarcated by black dashed lines (Figure 4). From bottom to top, these three regions represent quiet-Sun (QS), quiet-Sun with Coronal Hole boundary (QSCH) and Coronal Hole (CH) respectively. The locations where we observe excess widths compared to its average

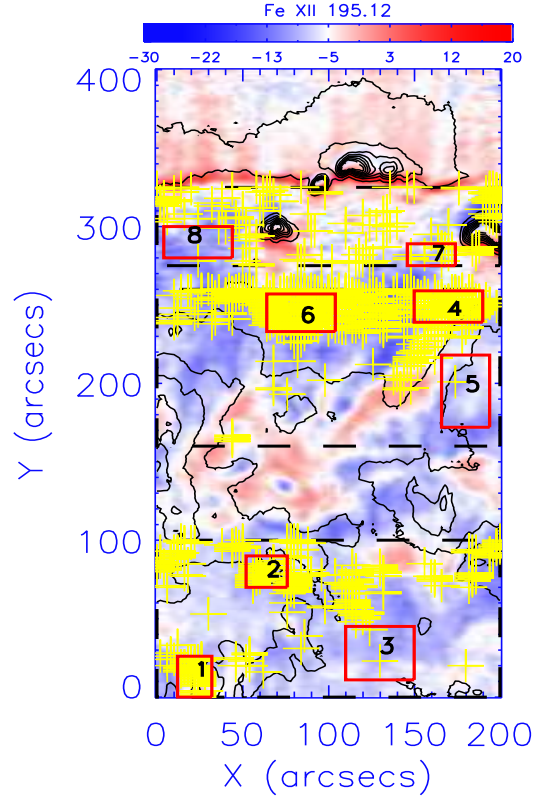


Figure 4. The image shows Doppler velocity map of the observed region, which is overlaid by intensity contours as well as excess width locations (marked by yellow plus symbols). All selected regions have been over-plotted on the Doppler velocity map by red rectangular boxes.

values in the neighbouring regions may allow us to locate these locations where various transients/explosive events are occurring. Furthermore, we have searched the excess width locations in all three regions by setting different threshold level in each box. Widths above the threshold levels have been considered as the excess widths. The average widths as well as the threshold levels in all the three regions (*i.e.*, QS, QSCH and CH) have been listed in Table 2. After finding the excess width locations, we have marked these locations over the Doppler velocity map by yellow plus signs (*cf.*, Figure 4). Finally, we have selected eight different boxes of different sizes in these three regions. Some boxes, out of these eight boxes, correspond to the excess width regions while rest of the boxes are located in the average width regions. All the eight selected boxes are overplotted on the same Doppler velocity map (*cf.*, Figure 4) by dark red color and are numbered. The description of all the selected regions (*i.e.*, three big boxes as well as eight small boxes) is given in Table 3. We have chosen these small eight regions to

Table 2. This table shows the average observed widths of all three region (i.e., QS, QSCH and CH). Similarly, the adopted threshold level of widths in each box to locate the excess widths in these regions have also been shown in this table.

Sr. No.	Big Black Dashed Box	Average Width (mÅ)	Threshold Width (mÅ)
1	QS	33.65	$1.20 \times \text{Average Width}$
2	QSCH	33.47	$1.30 \times \text{Average Width}$
3	CH	39.42	$1.35 \times \text{Average Width}$

compare various parameters corresponding to the excess width locations with the locations having average width below the threshold values. On the basis of this comparison, we have performed a comparison between QS and CH as well as tried to locate the coronal funnels in QS, QSCH and CH.

Table 3. The table gives the details about the all selected boxes, which is used in the present analysis.

Description of different selected regions		
Big Black Dashed Boxes	Small Boxes	Description
QS (Lower Box)	Box 1	Excess Width
	Box 2	Excess Width
	Box 3	Average Width
QSCH (Middle Box)	Box4	Excess Width
	Box 5	Average Width
	Box 6	Excess Width
Coronal Hole (Upper Box)	Box 7	Excess Width
	Box 8	Average Width

3.1. Doppler Velocity Variations

Investigation of the variation of Doppler velocity with temperature reveals the nature of plasma flow (*i.e.*, up-flows/down-flows) in the solar atmosphere. The lines, which we have used in the present study, cover the TR (Si VII 275.35 Å, $\text{Log } T_e = 5.8$ K) up to the solar corona (Fe XIII 202.04 Å, $\text{Log } T_e = 6.2$ K), corresponding to the QS (upper left, Figure 5), QSCH (upper right, Figure 5) and CH (bottom left, Figure 5). The overall trend is shown in the right panel of Figure 5. The Doppler velocities corresponding to the observed excess width regions of QS (*i.e.*, Box 1 and 2) are $\sim 0.26 \pm 0.27$ and $\sim -2.44 \pm 0.20$ km s⁻¹ at Si VII formation temperature, therefore, these excess width regions show marginal up-flows in upper TR. The plasma up-flows in these excess width regions increases with temperature up to the corona, which have maximum Doppler velocity of $\sim -9.42 \pm 0.14$ km s⁻¹ and $\sim -10.07 \pm 0.14$ km s⁻¹ in both

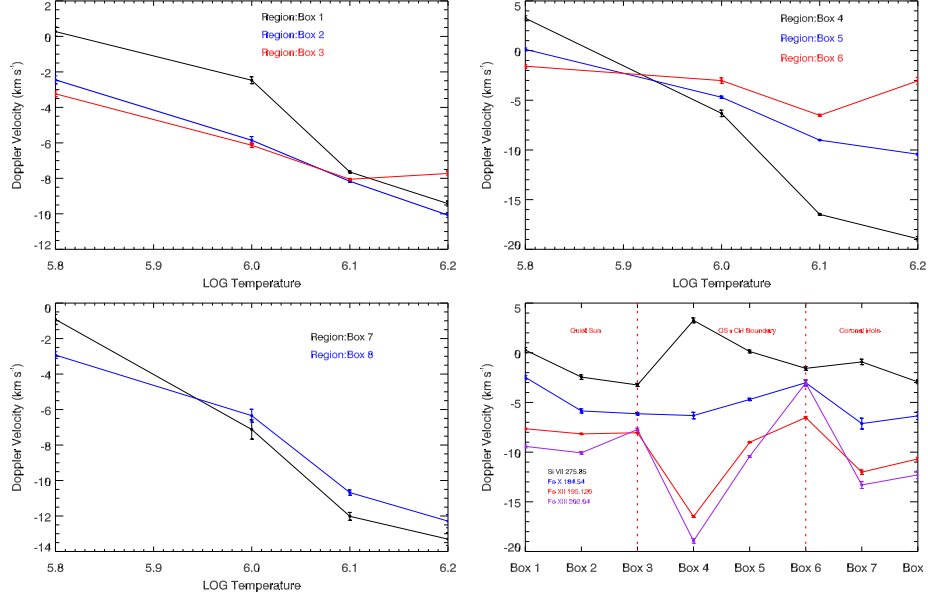


Figure 5. Doppler velocity variations with temperature corresponding to different regions QS (top-left), QSCH (top-right) and CH (bottom-left). The overall trend is shown in bottom-right panel.

excess width regions (*i.e.*, Box 1 and 2) at the temperature $\text{Log } T_e = 6.2 \text{ K}$ (*cf.*, Figure 5). The Doppler velocity of Box 3, which is located in the average width region of QS, is $\sim -3.24 \pm 0.16 \text{ km s}^{-1}$ at Si VII ion formation temperature, which increases further in the solar atmosphere up to Fe XII formation temperature with the blue-shift value $\sim -8.05 \pm 0.05 \text{ km s}^{-1}$. However, at the Fe XIII 202.04 Å ion formation temperature, this region shows slight decrease in the blue-shift (*i.e.*, $-7.7 \pm 0.13 \text{ km s}^{-1}$). The reduction in blue-shift at Fe XIII 202.04 Å from Fe XII 195.120 Å is not very high in this average width region of QS, although, blue-shift may decrease further towards higher heights in the solar atmosphere. Therefore, we can say that the Doppler velocity in the average width region of QS (Box 3) may have a different nature from the Doppler velocity nature of excess width regions of the QS (Box 1 and 2). It should be noted that we are trying to identify these excess width regions as the footprints of coronal funnels, which should show predominance of either wave activity and/or flows.

Similar to the QS region, in the QSCH region (upper-right snapshot, Figure 5), we have also selected three boxes for similar purpose. Boxes 4 and 6 are located in the excess width regions while Box 5 corresponds to the average width region (*cf.*, Table 3). Box 4, which is located at the boundary of CH, shows down-flows (*i.e.*, red-shifts) at TR and as the temperature increases the red-shift inverts into blue-shift with the maximum value of $\sim -18.93 \pm 0.23 \text{ km s}^{-1}$ at $\text{Log } T_e = 6.2 \text{ K}$. On contrary, the Doppler velocity of Box 6, which is also an excess width region, does not change very much from Si VII 275.35 Å ion ($-1.57 \pm 0.18 \text{ km s}^{-1}$) to Fe XIII 202.04 Å ($-3.04 \pm 0.34 \text{ km s}^{-1}$). Therefore, the Doppler velocity is almost constant in this box from TR up to the solar corona. The Doppler

velocity of Box 5, which is an average width QS region near CH boundary, is weakly red-shifted ($0.13 \pm 0.14 \text{ km s}^{-1}$) at $\text{Log } T_e = 5.8 \text{ K}$. After that the up-flow speed increases with temperature with a maximum value of $-10.43 \pm 0.09 \text{ km s}^{-1}$ at $\text{Log } T_e = 6.2 \text{ K}$. Therefore, it is very difficult to make distinction between the excess and average width regions on the basis of the net Doppler velocities in the QSCH regions.

Excess width (Box 7) and average width (Box 8) regions of CH (*cf.*, Table 3) have the Doppler velocities of $-0.92 \pm 0.28 \text{ km s}^{-1}$ and $-2.93 \pm 0.19 \text{ km s}^{-1}$ in Si VII at $\text{Log } T_e = 5.8$, respectively. The blue-shifts increase with temperature in both the regions and the maximum values of blue shifts are $-13.30 \pm 0.35 \text{ km s}^{-1}$ and $-12.29 \pm 0.38 \text{ km s}^{-1}$ in these excess as well as average width boxes at $\text{Log } T_e = 6.2 \text{ K}$. Again, it is very difficult to distinguish excess width location (Box 7) from average width location (Box 8) because both types of regions show similar pattern of the Doppler velocity. One can conjecture that it may be that corresponding to CHs the funnels have expanded so much at these heights, therefore, one can not distinguish a funnel and inter funnel regions.

The overall comparison of Doppler velocity of each emission line in all the eight boxes (Bottom right panel of Figure 5) shows that coolest line (*i.e.*, Si VII 275.35 \AA , $\text{Log } T_e = 5.8 \text{ K}$) is slightly blue-shifted in the QS, QSCH and CH. Although, the Box 5, which is located at the boundary of CH and QS (see Figure 4), shows larger red-shift at this temperature. The higher temperature lines (*i.e.*, Fe X 184.54 \AA , Fe XII 195.120 \AA and Fe XIII 202.04 \AA) move towards the higher blue-shifts as the temperature rises. Therefore, the cool line is dominated by down-flows, while the hot lines are dominated by up-flows as already been reported in the literatures (*cf.*, Figure 6).

The average Doppler shift of spectral lines formed from chromosphere to the corona reveal important information on the mass and energy balance of the solar atmosphere. We compare our results with previously published net Doppler shift values (*cf.*, Figure 6), corresponding to the quiet-Sun for various TR and coronal lines as recorded by SUMER and EIS spectra. Positive values indicate red-shifts (down-flows), while the negative values indicate blue-shifts (up-flows). The QS Doppler velocities, which we have obtained in the present work by using Hinode/EIS spectrum, are marked by red-star symbols. We should also point out that absolute values of the Doppler velocities depend on the rest wavelength and the measurement of the rest wavelength is very crucial. As we have described earlier in Section 2 that we have used the limb method (Peter and Judge, 1999; Dammasch *et al.*, 1999) to calculate the accurate rest wavelengths of the used EIS lines. In the limb method, it is assumed that the average Doppler velocity is almost zero around the solar limb (*i.e.*, motions along the line of sight cancel out on average in an optically thin plasma). For the 4th order polynomial fit (solid black line) from chromosphere to the corona, we have include results from Teriaca, Banerjee, and Doyle 1999a.

3.2. Electron Density Variations

The best available density sensitive Fe XII line pair has been used for the density measurement (Section 2). The left panel of Figure 7 represents the density map of

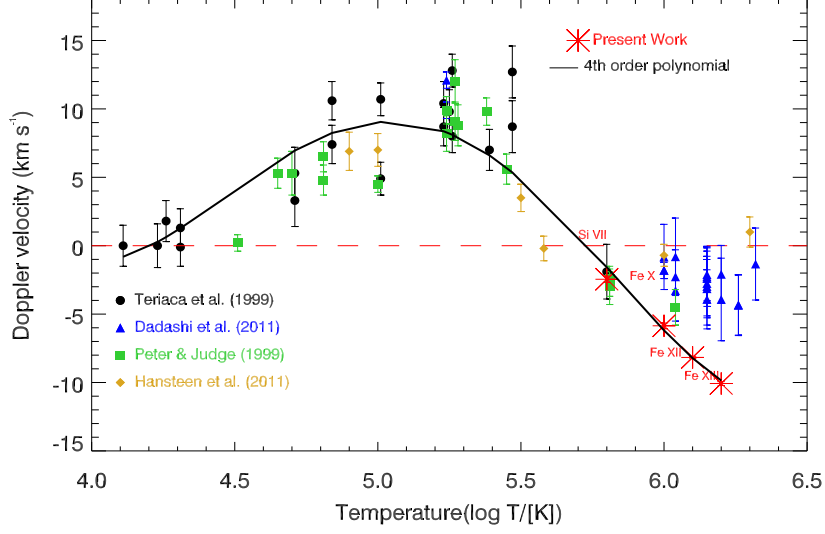


Figure 6. Average Doppler shift in the QS at disk center corresponding to various TR and CH ions as measured by SUMER and EIS spectra and as reported by earlier works as labeled. Our estimated Doppler velocity results of QS are marked by red-star symbols. Positive values indicate red-shifts (down-flows), while negative values indicate blue-shifts (up-flows). The solid line represents a fourth order polynomial fit to the data.

the observed region while the right panel shows averaged density corresponding to the three QS boxes, three QSCH boxes and two CH boxes (for box description; see Section 3). The density decreases progressively from QS to CH (*cf.*, right panel; Figure 7), which is expected. In the QS region, the electron densities of the excess width boxes (*i.e.*, Box 1 and 2) are $\text{Log } N_e = 8.63 \text{ cm}^{-3}$ and $\text{Log } N_e = 8.60 \text{ cm}^{-3}$ respectively, while the electron density of the average width box (*i.e.*, Box 3) is $\text{Log } N_e = 8.47 \text{ cm}^{-3}$. Therefore, the excess width boxes have the higher electron densities in comparison to the density of average width box within QS.

In QSCH region (*cf.*, QS+CH dashed box of right panel of Figure 7), the electron density of the excess width boxes (*i.e.*, Box 4 and 6) are $\text{Log } N_e = 8.30 \text{ cm}^{-3}$ and $\text{Log } N_e = 8.33 \text{ cm}^{-3}$ respectively, while the electron density of average width box (*i.e.*, Box 5) is $\text{Log } N_e = 8.45 \text{ cm}^{-3}$. The electron density of average width box is high in comparison to the excess width boxes because the average width box is located in the quiet-Sun while the excess width boxes are located in the Qs-CH and CH regions. Coronal hole boundaries are the most probable locations of various explosive events (Madjarska, Doyle, and van Driel-Gesztelyi, 2004; Madjarska and Wiegmann, 2009; Madjarska *et al.*, 2012), therefore, we expect that the excess width as well as high density locations lie along the coronal hole boundaries. Excess widths are present along the coronal hole boundary (*cf.*, yellow plus signs in Figure 4). Although, the density of Box 4 that covers

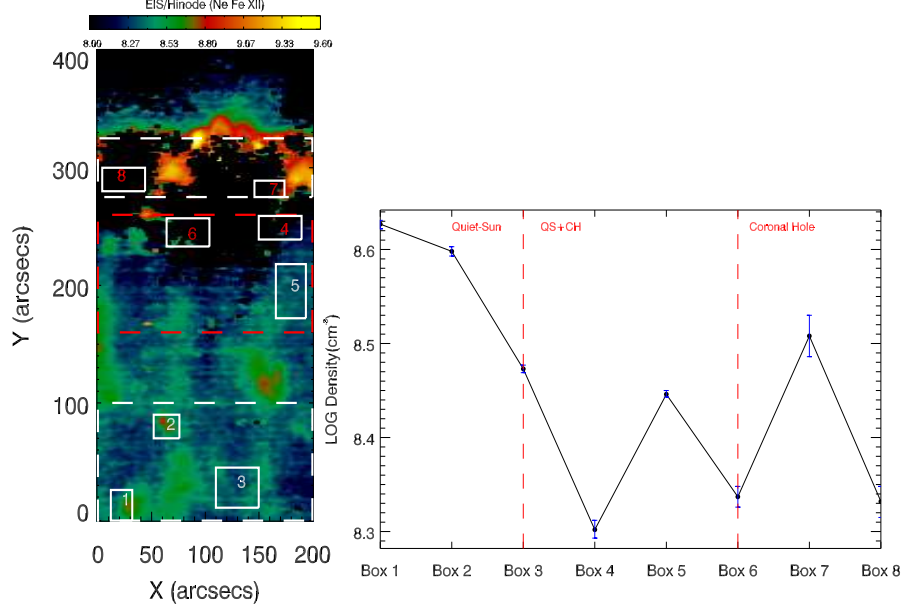


Figure 7. The electron density map of the observed (left panel). The small selected regions are overplotted on the electron density map by white rectangular boxes. The averaged electron densities of all boxes are shown in the right panel.

the coronal hole boundary along with large portion of the coronal hole, does not represent high density compared to the density of the box completely lying within coronal hole (*i.e.*, Box 6). Presence of the higher density (left panel of Figure 7) as well as maximum number of excess width pixels within Box 6 are to be noted. In CH, the density of the excess (Box 7) and average (Box 8) width locations are $\text{Log } N_e = 8.50 \text{ cm}^{-3}$ and $\text{Log } N_e = 8.34 \text{ cm}^{-3}$ respectively. The higher electron density corresponding to the excess width box (Box 7) may be influenced by the presence of a bright point (see left panel of Figure 7). Therefore, if we neglect the presence of the high density regions from the Box 5 and Box 7, then we can assume that the electron density of all excess and average width boxes located in coronal hole (*i.e.*, Box 4, 6, 7 and 8) are almost same. On the basis of the electron density, it is not possible to make distinction between excess and average width regions of CH and QSCH.

4. Temperature Dependent Behaviour of Non-Thermal Velocity in QS

Non-thermal velocities can provide information about the unresolved motions/MHD waves in the solar atmosphere. Instrumental, thermal and non-thermal widths are the three component of the observed line width. Therefore, to get non-thermal width, the removal of the instrumental and thermal widths from the

line width has been performed by using following formula,

$$W_{nt} = [W_{obs}^2 - W_{inst}^2 - W_{th}^2]^{1/2}, \quad (2)$$

where, W_{nt} , W_{obs} , W_{inst} and W_{th} are non-thermal, observed, instrumental and thermal widths respectively. The on-average instrumental width (i.e., W_{inst}) is ~ 66 mÅ while the thermal width can be calculated using the relation,

$$W_{th} = 4 \ln 2 \left(\frac{\lambda}{c} \right)^2 \left[\frac{2kT_i}{M_i} \right]. \quad (3)$$

After estimating non-thermal widths, we have calculated the non-thermal velocities of QS and CH for Si VII 275.35 Å, Fe XII 195.120 Å and Fe XIII 202.04 Å lines. The non-thermal velocity is calculated from this equation,

$$\xi = \left(\frac{W_{nt}^2 c^2}{4 \ln 2 \lambda^2} \right)^{1/2} \quad (4)$$

QS region non-thermal velocities of Si VII, Fe XII and Fe XIII lines have been

Table 4. Quiet Sun Non-thermal Velocity ξ (km s⁻¹)

Box number	Si VII	Fe XII	Fe XIII
1	23.64±0.35	28.76±0.07	22.23±0.02
2	24.34±0.28	31.48±0.07	20.09±0.17
3	27.64±0.21	31.45±0.05	20.92±0.16

listed in Table 4 while the CH non-thermal velocities have been listed in the Table 5. The non-thermal velocities follow the same pattern in all selected boxes (i.e., located in QS and CH regions) within the narrow temperature range (from Si VII up to Fe XIII ion temperature) in the solar atmosphere. The non-thermal

Table 5. Coronal Hole Non-thermal Velocity ξ (km s⁻¹)

Box number	Si VII	Fe XII	Fe XIII
7	33.28±0.35	37.83±0.26	24.26±0.44
8	31.13±0.24	37.76±0.18	26.72±0.49

velocity increase from Si VII up to the Fe XII and after that it decreases towards Fe XIII ion in the all selected boxes. We have included previous results as reported in Doschek *et al.* (1976); Mariska, Feldman, and Doschek (1978); Dere and Mason (1993); Chae, Yun, and Poland (1998). This plot covers a large portion of the solar atmosphere and allows us to compare our results with previous numbers. It also provides a new unified physical scenario in the solar atmosphere which shows how the non-thermal velocity behave between $4.0 \text{ K} \leq \text{Log } T_e \leq 6.2$

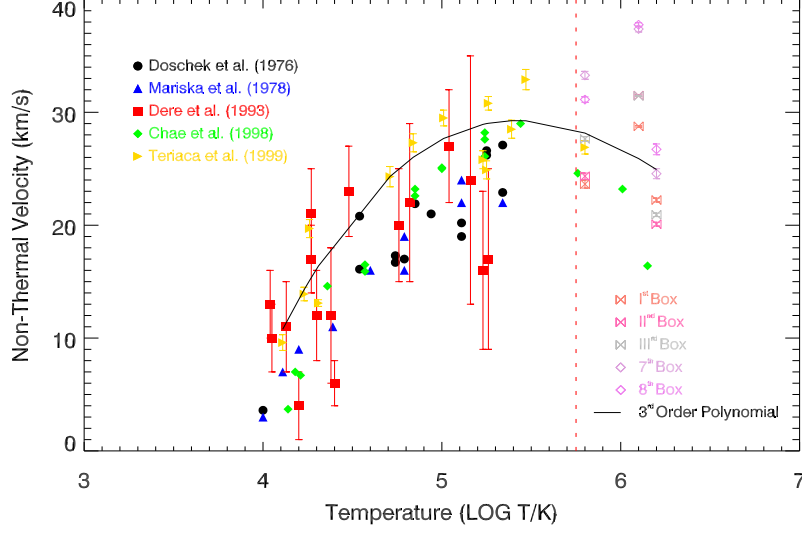


Figure 8. Variation of the non-thermal velocities with temperature corresponding to the QS. To cover a wide range of temperatures, we have included previous results as labeled. Using non-thermal velocities reported by Teriaca, Banerjee, and Doyle 1999a and derived from Box 3, we have fitted a 3rd order polynomial as shown by solid black line. Our estimated results of QS and CH boxes are plotted to the right side of the red vertical dashed line.

K, *i.e.*, covering from chromosphere, TR, corona above QS. The behaviour of non-thermal velocity with temperature in all selected QS (*i.e.*, 1st, 2nd and 3rd) boxes along with previous results has been shown in Figure 8. We have also plotted the non-thermal velocities of CH boxes (*i.e.*, 7th and 8th boxes) in the same plot. We found that non-thermal velocities first rise up, attains a maximum value, and thereafter decreases further in the solar atmosphere (*i.e.*, quiet-Sun here). A 3rd order polynomial, using our QS non-thermal velocity (*i.e.*, Box 3) and non-thermal velocity by Teriaca, Banerjee, and Doyle (1999a), has been fitted. This shows that the non-thermal velocity peaks at $\text{Log } T_e \sim 5.47$ K and after that the on-average non-thermal velocity decreases in the QS.

5. Discussion and Conclusions

In the present work, we have studied the polar coronal hole and adjacent quiet-Sun, as observed on 10 October 2007 by *Hinode*/EIS. Using *Hinode*/EIS spectra, a comparison between QS and CH has been performed. In the present study, we found that on average the line width of CH (39.42 mÅ) is higher in comparison to the line width of QS (33.65 mÅ, *cf.*, Table 2). Even, after setting a higher threshold limit of the line widths in CH (*i.e.*, 1.35×CH average line width) in comparison to the QS threshold line width limit (*i.e.*, 1.20×QS average width) to locate excess width locations in CH and QS, we found that CH has larger

number of excess width locations in comparison to the excess width locations in QS (see Figure 4). We assumed that excess width locations may correspond to regions where various type of transients/explosive events may occur in solar atmosphere. Variations in the line width is directly related to the variations of the non-thermal width component (Section 3), therefore, the CH has higher non-thermal width as well as large number of excess non-thermal width locations in comparison to the QS. As we know that CHs are the source regions of the fast solar wind (Krieger, Timothy, and Roelof, 1973; Tu *et al.*, 2005; Kohl *et al.*, 2006; He, Tu, and Marsch, 2008; Tian *et al.*, 2010) as well as the sites for oscillation and various type of MHD waves (Banerjee *et al.*, 2001a,b; O’Shea, Banerjee, and Doyle, 2006, 2007; Banerjee, Pérez-Suárez, and Doyle, 2009; Gupta *et al.*, 2010; Krishna Prasad, Banerjee, and Gupta, 2011). Therefore, the presence of the larger non-thermal width and large number of excess width locations in the CH in comparison to the QS is quite obvious due to the presence of these flows/waves in the CH.

It is now well established that the lower temperature lines are dominated by down-flows while higher temperature lines are dominated by blue-shifts in QS and CH (Chae, Yun, and Poland, 1998; Peter and Judge, 1999; Teriaca, Banerjee, and Doyle, 1999a; Tian *et al.*, 2008a,c; Hansteen *et al.*, 2010; Tian *et al.*, 2010; Dadashi, Teriaca, and Solanki, 2011). Therefore, there is transition from red-shift to blue-shift at some temperature, which is an important observational parameter from the point of view of the TR models. Excess width regions of QS are slightly blue-shifted at $\text{Log } T_e = 5.8$ K (*i.e.*, Si VII 275.35 Å), therefore, the inversion from red-shift to blue-shift has already been taken place below the $\text{Log } T_e = 5.8$. On the basis of observed blue-shift (-1.9 ± 2.0 km s $^{-1}$) of the Ne VIII 770.428 Å line as seen by SUMER, which has a temperature similar to the temperature of Si VII line, Peter and Judge (1999) have already been inferred that such transition occur at $\text{Log } T_e = 5.7$ K in QS. Therefore, we can also conclude that transition (*i.e.*, from red-shift to blue-shift) also takes place at the same temperature in these excess width regions of the QS. Similar to excess width regions of QS, the average and excess width regions (*i.e.*, box, 6, 7 and 8) of CH also show marginal blue-shifts at $\text{Log } T_e = 5.8$ K. Therefore, we can infer that transition temperature in CH is similar to the QS. Although, one CH box (*i.e.*, Box 4), which is located at the coronal hole boundary, shows strong red-shift at $\text{Log } T_e = 5.8$ K. This region might have been influenced by large number of explosive events. The properties of the excess width regions of the QS are similar to CH (*i.e.*, excess and average width regions), but, the densities of the excess width regions of QS are higher in comparison to the CH. In contrast, one average width box (Box 3) of QS does not show the continuous plasma up-flows while another average width box (Box 5) shows continuous plasma up-flows. Similarly, Box 3 and 5 show strong blue-shift (-3.24 km s $^{-1}$) and weak red-shift ($+0.13$ km s $^{-1}$) at $\text{Log } T_e = 5.8$, therefore, we can not deduce a common transition temperature for these average width regions of QS. As we know that the coronal funnels as well as small and large magnetic loops are the basic building blocks of the solar atmosphere. The upper TR line blue-shifts patches are associated with coronal funnels (Tu *et al.*, 2005), although, these blue-shift patches may be associated with the magnetic loops as well. As we

have shown earlier that QS excess width boxes show continuous plasma up-flows while QS average width region does not represent the continuous plasma up flows. Similarly, the averaged densities of QS excess width regions are higher in comparison to the average width region of QS, although, the density difference is not very much. We should note that we are measuring the electron density on the basis of the intensity ratio of Fe XII line, which represents the electron density at coronal heights. At the coronal heights, due the large expansion of the coronal funnels, the electron density in the coronal funnels may not be different significantly from the surrounding region. Therefore, slightly higher densities as well as presence of continuous plasma up-flows in the excess width regions of QS provide sufficient signature to identify that these excess width locations in QS are associated with the coronal funnels. On the basis of Doppler velocity, excess width and density, we can not distinguish the excess width boxes from the average width boxes in QSCH and CH. As we know that QS are mostly dominated by coronal loops and only a small fraction of the QS area is occupied by coronal funnels while the CH are mostly dominated by coronal funnels (Peter, 2001). Therefore, we have easily located the coronal funnels in QS but it is very hard to isolate the footprints of the coronal funnels within coronal holes. It may be possible that all selected boxes in CH (*i.e.*, excess and average) are coronal funnel occupied regions because of large filling factor. We can propose that the plasma flow inversion (*i.e.*, inversion from down-flows to up flows) takes place at $\text{Log } T_e = 5.7 \text{ K}$ in CH. Similarly, the inversion of plasma flow also takes place at the same temperature ($\text{Log } T_e = 5.7 \text{ K}$) in excess width regions of QS. However, the average width regions of the QS do not show similar pattern of the Doppler velocity, therefore, it is hard to get conclusive plasma flow inversion temperature in these average width regions of QS. Finally, we found that excess width regions of QS show continuous plasma up-flows as well as high density concentration while the average width region of QS does not follow continuous plasma flow pattern and the density of the average width region is lower in comparison to the excess width regions of QS. Therefore, the excess width regions are the most probable locations of coronal funnels in QS, however, we could not locate the footprints of coronal funnels in the QSCH and CH using the same procedure. As we know that the coronal holes are dominated by open magnetic filed lines, therefore, it may be possible that all the selected regions of QSCH and CH (except Box 5) at these heights are within coronal funnels because in CH the parameters are similar within funnel and the adjacent background region.

Apart from this, Doppler shift of TR and coronal lines has been also investigated while combining our results with previously reported numbers from SUMER (*cf.*, Figure 6). This new plot now covers a wide range of temperature from chromosphere up to high corona. Doppler velocity inversion from red-shift to blue-shift takes place around $\text{Log } T_e = 5.7 \text{ K}$ (see the peak of 4th order polynomial fit in Figure 6), which is in good agreement with earlier results (Peter and Judge, 1999; Teriaca, Banerjee, and Doyle, 1999a). Recently Fu *et al.* (2014) have measured the Doppler velocity variations with temperature in the same NPCH area, however, they have focused on the on-disk plume structures. We feel that these plume structures could be also used as tracers of coronal funnels. Some of their results complement results presented here. Our focus has been

on the line widths rather than the outflow velocities alone. Earlier, 1-D models which assumes energy release in magnetic loops had successfully managed to reproduce the observed red-shift at TR temperatures and blue-shifts at coronal temperatures (Teriaca *et al.*, 1999b; Spadaro *et al.*, 2006). However, these models do not explicitly consider the heating mechanisms. More recently, Srivastava *et al.* (2014) presented numerical model in 2-D realistic solar atmosphere, the generation of the blue-shifts (out-flows) due to heating pulses, as observed by Hinode/EIS at coronal temperature. Peter, Gudiksen, and Nordlund (2004, 2006) presented, 3D models assuming that the coronal heating is caused by joule dissipation of currents produced by stressing and braiding of the magnetic fields produce red-shifts at all temperatures. Episodic injection of emerging magnetic flux, which reconnects with the existing field, produces rapid, episodic heating of the upper chromospheric plasma to coronal temperatures (Hansteen *et al.*, 2010). Dadashi, Teriaca, and Solanki (2011) measured the averaged Doppler shifts from 0.01 up to 2.1 MK and they have shown that 3D coronal models are more appropriate for the explanation of the observed Doppler velocity pattern from chromosphere up to the corona.

The inhomogeneous solar plasma should support different MHD modes as well as acoustic wave and this has been confirmed by observations and theory (Ofman and Davila, 1997; DeForest and Gurman, 1998; Banerjee *et al.*, 2001a,b; O'Shea, Banerjee, and Doyle, 2006; Dwivedi and Srivastava, 2006; Srivastava and Dwivedi, 2007; O'Shea, Banerjee, and Doyle, 2007; Banerjee, Pérez-Suárez, and Doyle, 2009; Gupta *et al.*, 2010; Krishna Prasad, Banerjee, and Gupta, 2011; Chmielewski *et al.*, 2013). It has been proposed that several mechanisms are responsible for the non-thermal broadening, *e.g.*, propagation of waves (Mariska, Feldman, and Doschek, 1978; Banerjee, Pérez-Suárez, and Doyle, 2009), non-thermal motions (Doschek *et al.*, 1976; Athay and Dere, 1991; Chae, Yun, and Poland, 1998), MHD turbulence (Gomez and Ferro Fontan, 1988, 1992; Heyvaerts and Priest, 1992) and nano-flare heating (Patsourakos and Klimchuk, 2006). In-spite of all these physical processes, the nature of the non-thermal broadening is not fully understood. We confirm here a more complete picture of the non-thermal velocity in the wide temperature range from $\sim 1.0 \times 10^4$ K to 1.58×10^6 (Figure 8). Initially, the non-thermal velocity increases with temperature but after certain TR temperature ($\text{Log } T_e = 5.8$ K) non-thermal velocity decreases further upto inner corona ($\text{Log } T_e = 6.2$ K). Undamped Alfvén waves are responsible for non-thermal broadening (Hassler *et al.*, 1990; Banerjee *et al.*, 1998; Wilhelm *et al.*, 2004, 2005; Banerjee, Pérez-Suárez, and Doyle, 2009), while narrowing of spectra after a certain height in the solar atmosphere is most likely signature of the Alfvén wave dissipation (Doyle *et al.*, 1997; Roberts, 2000; Pekünlü *et al.*, 2002; O'Shea, Banerjee, and Doyle, 2005). Therefore, propagation of Alfvén waves increases the non-thermal velocity up to the inversion point in QS ($\text{Log } T_e = 5.47$ K) and after the inversion point, which lies in the upper TR/lower corona, Alfvén waves may dissipate through various mechanisms, *e.g.*, viscous & ohmic (Roberts, 2000), resonant absorption (Ionson, 1978; Erdelyi and Goossens, 1996; Doyle *et al.*, 1997), phase mixing, *etc.* Although, which mechanism is responsible for the Alfvén wave dissipation can

not be speculated here. This is one possible explanation for our results related to the non-thermal velocity pattern in QS. Apart from the Alfvén wave propagation and dissipation mechanism, another possible explanation may lie in terms of the nano-flares, which is frequently occurring at O VI temperature (Peter and Judge, 1999). Teriaca *et al.* 2004 reported that non-thermal velocity peak is at the same O VI formation temperature (*i.e.*, $3 \times 10^5 K$) and they concluded that non-thermal velocities arise due to the prevalent occurrence of the nano-flares in this region. The presence of the lower values of non-thermal velocities above and below this region is quite obvious due to the energy loss. In the present case, the non-thermal velocity peaks at $\text{Log } T_e = 5.47 \text{ K}$ ($2.95 \times 10^5 \text{ K}$) in the QS. Therefore, our peak value of the non-thermal velocity is also very close to the O VI formation temperature and it may be probable justification for our non-thermal results. In conclusion, Alfvén wave propagation and dissipation as well as prevalent occurrence of the nano-flares around at O VI formation temperature can explain the variation of non-thermal velocity with temperature. These two mechanisms are the viable source but that does not rule out other possibilities. Our results should help in constraining the atmospheric models. We hope that our attempt of identifying the footprints of coronal funnels based on density contrast and excess widths shed new light on the overall complexity and topology of the polar regions in general. This approach of searching for additional widths as precursors for transients can be further improved with future better resolution spectrographs.

Acknowledgements We acknowledge the Hinode/EIS observation for this study. Hinode is Japanese mission developed and launched by ISAS/JAXA, with NAOJ as domestic partner and NASA and UKSA as international partners. P. Kayshap acknowledges the support from Indian Institute of Astrophysics, Bangalore for his visit.

References

- Aiouaz, T., Peter, H., and Lemaire, P.: 2005, *Astron. Astroph.* **435**, 713.
 Athay, R.G.: 1984, *Astrophys. J.* **287**, 412.
 Athay, R.G. and Dere, K.P.: 1991, *Astrophys. J.* **381**, 323.
 Axford, W.I. and McKenzie, J.F.: 1997, *Cosmic Winds and the Heliosphere*, 31.
 Banerjee, D., Teriaca, L., Doyle, J.G., and Wilhelm, K.: 1998, *Astron. Astroph.* **339**, 208.
 Banerjee, D., O’Shea, E., Doyle, J.G., and Goossens, M.: 2001a, *Astron. Astroph.* **377**, 691.
 Banerjee, D., O’Shea, E., Doyle, J.G., and Goossens, M.: 2001b, *Astron. Astroph.* **380**, L39.
 Banerjee, D., Pérez-Suárez, D., and Doyle, J.G.: 2009, *Astron. Astroph.* **501**, L15.
 Boland, B.C., Dyer, E.P., Firth, J.G., Gabriel, A.H., Jones, B.B., Jordan, C., McWhirter, R.W.P., Monk, P., and Turner, R.F.: 1975, *Monthly Notices of the Royal Astronomical Society* **171**, 697.
 Chae, J., Schühle, U., and Lemaire, P.: 1998, *Astrophys. J.* **505**, 957.
 Chae, J., Yun, H.S., and Poland, A.I.: 1998, *The Astrophysical Journal Supplement Series* **114**, 151.
 Chmielewski, P., Srivastava, A.K., Murawski, K., and Musielak, Z.E.: 2013, *Monthly Notices of the Royal Astronomical Society* **428**, 40.
 Coyner, A.J. and Davila, J.M.: 2011, *Astrophys. J.* **742**, 115.
 Culhane, J.L., Harra, L.K., James, A.M., Al-Janabi, K., Bradley, L.J., Chaudry, R.A., Rees, K., Tandy, J.A., Thomas, P., Whillock, M.C.R., Winter, B., Doschek, G.A., Korendyke, C.M., Brown, C.M., Myers, S., Mariska, J., Seely, J., Lang, J., Kent, B.J., Shaughnessy, B.M., Young, P.R., Simnett, G.M., Castelli, C.M., Mahmoud, S., Mapson-Menard, H., Probyn,

- B.J., Thomas, R.J., Davila, J., Dere, K., Windt, D., Shea, J., Hagood, R., Moye, R., Hara, H., Watanabe, T., Matsuzaki, K., Kosugi, T., Hansteen, V., and Wikstol, Ø.: 2007, *Solar Phys.* **243**, 19.
- Dadashi, N., Teriaca, L., and Solanki, S.K.: 2011, *Astron. Astroph.* **534**, A90.
- Dammasch, I.E., Wilhelm, K., Curdt, W., and Hassler, D.M.: 1999, *Astron. Astroph.* **346**, 285.
- DeForest, C.E. and Gurman, J.B.: 1998, *Astrophys. J.* **501**, L217.
- Dere, K.P. and Mason, H.E.: 1993, *Solar Phys.* **144**, 217.
- Dere, K.P., Landi, E., Mason, H.E., Monsignori Fossi, B.C., and Young, P.R.: 1997, *Astronomy and Astrophysics Supplement Series* **125**, 149.
- Doschek, G.A., Vanhoosier, M.E., Bartoe, J.-D.F., and Feldman, U.: 1976, *The Astrophysical Journal Supplement Series* **31**, 417.
- Doschek, G.A. and Feldman, U.: 2000, *Astrophys. J.* **529**, 599.
- Doschek, G.A., Mariska, J.T., Warren, H.P., Brown, C.M., Culhane, J.L., Hara, H., Watanabe, T., Young, P.R., and Mason, H.E.: 2007, *Astrophys. J.* **667**, L109.
- Doyle, J.G., O'Shea, E., Erdelyi, R., Dere, K.P., Socker, D.G., and Keenan, F.P.: 1997, *Solar Phys.* **173**, 243.
- Dwivedi, B.N. and Srivastava, A.K.: 2006, *Solar Phys.* **237**, 143.
- Erdelyi, R. and Goossens, M.: 1996, *Astron. Astroph.* **313**, 664.
- Fu, H., Xia, L., Li, B., Huang, Z., Jiao, F., and Mou, C.: 2014, *ArXiv e-prints*, arXiv:1408.5473.
- Gabriel, A.H.: 1976, *Royal Society of London Philosophical Transactions Series A* **281**, 339.
- Gomez, D. and Ferro Fontan, C.: 1988, *Solar Phys.* **116**, 33.
- Gomez, D.O. and Ferro Fontan, C.: 1992, *Astrophys. J.* **394**, 662.
- Gupta, G.R., Banerjee, D., Teriaca, L., Imada, S., and Solanki, S.: 2010, *Astrophys. J.* **718**, 11.
- Hackenberg, P., Mann, G., and Marsch, E.: 1999, *Space Science Reviews* **87**, 207.
- Hansteen, V.: 1993, *Astrophys. J.* **402**, 741.
- Hansteen, V., Maltby, P., and Malagoli, A.: 1997, *Magnetic Reconnection in the Solar Atmosphere* **111**, 116.
- Hansteen, V.H., Hara, H., De Pontieu, B., and Carlsson, M.: 2010, *Astrophys. J.* **718**, 1070.
- Hassler, D.M., Dammasch, I.E., Lemaire, P., Brekke, P., Curdt, W., Mason, H.E., Vial, J.-C., and Wilhelm, K.: 1999, *Science* **283**, 810.
- Hassler, D.M., Rottman, G.J., Shoub, E.C., and Holzer, T.E.: 1990, *Astrophys. J.* **348**, L77.
- He, J.-S., Tu, C.-Y., and Marsch, E.: 2008, *Solar Phys.* **250**, 147.
- Heyvaerts, J. and Priest, E.R.: 1992, *Astrophys. J.* **390**, 297.
- Ionson, J.A.: 1978, *Astrophys. J.* **226**, 650.
- Kohl, J.L., Noci, G., Cranmer, S.R., and Raymond, J.C.: 2006, *Astronomy and Astrophysics Review* **13**, 31.
- Krieger, A.S., Timothy, A.F., and Roelof, E.C.: 1973, *Solar Phys.* **29**, 505.
- Krishna Prasad, S., Banerjee, D., and Gupta, G.R.: 2011, *Astron. Astroph.* **528**, L4.
- Landi, E., Del Zanna, G., Young, P.R., Dere, K.P., Mason, H.E., and Landini, M.: 2006, *The Astrophysical Journal Supplement Series* **162**, 261.
- Madjarska, M.S., Doyle, J.G., and van Driel-Gesztelyi, L.: 2004, *Astrophys. J.* **603**, L57.
- Madjarska, M.S. and Wiegmann, T.: 2009, *Astron. Astroph.* **503**, 991.
- Madjarska, M.S., Huang, Z., Doyle, J.G., and Subramanian, S.: 2012, *Astron. Astroph.* **545**, A67.
- Mariska, J.T., Feldman, U., and Doschek, G.A.: 1978, *Astrophys. J.* **226**, 698.
- Marsch, E. and Tu, C.-Y.: 1997, *Solar Phys.* **176**, 87.
- McIntosh, S.W., Davey, A.R., Hassler, D.M., Armstrong, J.D., Curdt, W., Wilhelm, K., and Lin, G.: 2007, *Astrophys. J.* **654**, 650.
- Ofman, L. and Davila, J.M.: 1997, *Astrophys. J.* **476**, L51.
- O'Shea, E., Banerjee, D., and Doyle, J.G.: 2005, *Astron. Astroph.* **436**, L35.
- O'Shea, E., Banerjee, D., and Doyle, J.G.: 2006, *Astron. Astroph.* **452**, 1059.
- O'Shea, E., Banerjee, D., and Doyle, J.G.: 2007, *Astron. Astroph.* **463**, 713.
- Patsourakos, S. and Klimchuk, J.A.: 2006, *Astrophys. J.* **647**, 1452.
- Pekünli, E.R., Bozkurt, Z., Afsar, M., Soyduğan, E., and Soyduğan, F.: 2002, *Monthly Notices of the Royal Astronomical Society* **336**, 1195.
- Peter, H. and Judge, P.G.: 1999, *Astrophys. J.* **522**, 1148.
- Peter, H.: 1999, *Astrophys. J.* **522**, L77.
- Peter, H.: 2001, *Astron. Astroph.* **374**, 1108.
- Peter, H., Gudiksen, B.V., and Nordlund, Å.: 2004, *Astrophys. J.* **617**, L85.
- Peter, H., Gudiksen, B.V., and Nordlund, Å.: 2006, *Astrophys. J.* **638**, 1086.

- Pneuman, G.W. and Kopp, R.A.: 1978, *Solar Phys.* **57**, 49.
- Roberts, B.: 2000, *Solar Phys.* **193**, 139.
- Spadaro, D., Lanza, A.F., Karpen, J.T., and Antiochos, S.K.: 2006, *Astrophys. J.* **642**, 579.
- Srivastava, A.K. and Dwivedi, B.N.: 2007, *Journal of Astrophysics and Astronomy* **28**, 1.
- Srivastava, A.K., Konkol, P., Murawski, K., Dwivedi, B.N., and Mohan, A.: 2014, *ArXiv e-prints*, arXiv:1407.7124.
- Teriaca, L., Banerjee, D., and Doyle, J.G.: 1999a, *Astron. Astroph.* **349**, 636.
- Teriaca, L., Doyle, J.G., Erdélyi, R., and Sarro, L.M.: 1999b, *Astron. Astroph.* **352**, L99.
- Teriaca, L., Banerjee, D., Falchi, A., Doyle, J.G., and Madjarska, M.S.: 2004, *Astron. Astroph.* **427**, 1065.
- Tian, H., Marsch, E., Tu, C.-Y., Xia, L.-D., and He, J.-S.: 2008a, *Astron. Astroph.* **482**, 267.
- Tian, H., Xia, L.-D., He, J.-S., Tan, B., and Yao, S.: 2008c, *Chinese Journal of Astronomy and Astrophysics* **8**, 732.
- Tian, H., Tu, C., Marsch, E., He, J., and Kamio, S.: 2010, *Astrophys. J.* **709**, L88.
- Tu, C.-Y., Zhou, C., Marsch, E., Xia, L.-D., Zhao, L., Wang, J.-X., and Wilhelm, K.: 2005, *Science* **308**, 519.
- Waldmeier, M.: 1975, *Solar Phys.* **40**, 351.
- Warren, H.P., Mariska, J.T., and Wilhelm, K.: 1997, *Astrophys. J.* **490**, L187.
- Wiegmann, T. and Solanki, S.K.: 2004, *Solar Phys.* **225**, 227.
- Wilhelm, K., Dammasch, I.E., Marsch, E., and Hassler, D.M.: 2000, *Astron. Astroph.* **353**, 749.
- Wilhelm, K., Dwivedi, B.N., Marsch, E., and Feldman, U.: 2004, *Space Science Reviews* **111**, 415.
- Wilhelm, K., Fludra, A., Teriaca, L., Harrison, R.A., Dwivedi, B.N., and Pike, C.D.: 2005, *Astron. Astroph.* **435**, 733.
- Xia, L.D., Marsch, E., and Curdt, W.: 2003, *Astron. Astroph.* **399**, L5.
- Young, P.R., Del Zanna, G., Mason, H.E., Dere, K.P., Landi, E., Landini, M., Doschek, G.A., Brown, C.M., Culhane, L., Harra, L.K., Watanabe, T., and Hara, H.: 2007, *Publications of the Astronomical Society of Japan* **59**, 857.
- Young, P.R., Watanabe, T., Hara, H., and Mariska, J.T.: 2009, *Astron. Astroph.* **495**, 587.